Strain and electric field tuning of semi-metallic character $WCrCO_2$ MXenes with dual narrow band gap

Journal of Physics: Condensed Matter

Strain and electric field tuning of semi-metallic character WCrCO₂ MXenes with dual narrow band gap

To cite this article before publication: Asadollah Bafekry *et al* 2020 *J. Phys.: Condens. Matter* in press https://doi.org/10.1088/1361-648X/ab8e88

Strain and electric field tuning of semi-metallic character $WCrCO_2$ MXenes with dual narrow band gap

A. Bafekry[1,2,*] B. Akgenc[3], M. Ghergherehchi[4], and F. M. Peeters[2]

[1]*Department of Physics, University of Guilan, 41335-1914 Rasht, Iran*
[2]*Department of Physics, University of Antwerp, Groenenborgerlaan 171, B-2020 Antwerp, Belgium*
[3]*Department of Physics, Kirklareli University, Kirklareli, Turkey*
[4]*College of Electronic and Electrical Engineering, Sungkyun kwan University, Suwon, Korea*

(Dated: April 21, 2020)

Motivated by the recent successful synthesis of double-M carbides, we investigate structural and electronic properties of WCrC and $WCrCO_2$ monolayers and the effects of biaxial and out-of plane strain and electric field using density functional theory. WCrC and $WCrCO_2$ monolayers are found to be dynamically stable. WCrC is metallic and $WCrCO_2$ display semi-metallic character with narrow band gap, which can be controlled by strain engineering and electric field. $WCrCO_2$ monolayer exhibits a dual band gap which is preserved in the presence of an electric field. The band gap of $WCrCO_2$ monolayer increases under uniaxial strain while it becomes metallic under tensile strain, resulting in an exotic 2D double semi-metallic behavior. Our results demonstrate that $WCrCO_2$ is a new platform for the study of novel physical properties in two-dimensional Dirac materials and which may provide new opportunities to realize high-speed low-dissipation devices.

I. INTRODUCTION

MAX phases are ternary carbides and nitrides which have the general formula of $M_{n+1}AX_n$ where M is transition metal atom, A is a group XIII or XIV element, and X is C and/or N. Layered MAX phases are chemically exfoliated into two-dimensional (2D) mono- and multilayers, named MXenes (3D MAX $\rightarrow$ 2D MXene) [1–6]. More than 70 MAX phases have been experimentally produced, and dozens more have been predicted theoretically, hereby MXenes are one of the fastest growing two-dimensional material (2DM) family [7–9]. Since the discovery of titanium carbide (Ti_3C_2) in 2011 [1], MXenes have gained popularity due to their high surface area, high electrical and metallic conductivity [10, 11], hydrophilic nature [12], flexibility [13, 14], surface functional possibilities [15] and intrinsic magnetism [16–19]. MXenes can be synthesized by extracting the A-group atomic layers (mostly group 13 and 14 elements of the periodic table) from MAX phases. MXenes have the formula of $M_{n+1}X_nT_n$ (M: transition metal atom, X: C and/or N, T: surface termination, e.g., -O, -OH, -F which are strongly bonded within the layered sheets, and are held together with weak van der Waals interaction.

It is well known that the electronic properties of 2D materials (2DM) can be tuned by applying strain or external electric field, functionalization, introducing defects and vacancies [20–23]. But there are only a few reports on electronic properties of double-M 2D MXenes which can be controlled by strain engineering and electric field [24–26]. Very recently, large area high quality 2D Mo_2C has been fabricated by using chemical vapour deposition (CVD) [27, 28]. Tungsten and chromium based MXenes (which are in the same column with molybdenum) have been theoretically studied. W_2C shows a non-magnetic ground state and a high negative Poisson's ratio in 2D form. The later may lead to numerous engineering applications as e.g. an auxetic material [29]. The auxeticity of W_2C disappears when -O, -OH, -F surface functional groups are introduced. Those functional groups break the strong W-*d*-orbitals and C-*p*-orbitals coupling [30]. Si *et al.* [16] proposed that Cr_2C exhibits half-metallic ferromagnetic behavior with a large half-metallic gap as large as 2.85 eV due to itinerant *d*-electrons of Cr which are 100% spin-polarized around the Fermi surface. They have also demonstrated a ferromagnetic to antiferromagnetic (FM-AFM) transition by surface functionalization with -Cl, -OH, -F and -H. The etching and ex-foliating properties of Cr_2AlC and Cr_2CO_2 and their electrocatalytic properties with and without carbon defects were studied by Cheng *et al.* They demonstrated that etching pristine Cr_2AlC by HF solution could generate Cr_2C MXenes with O* termination: Cr_2CO_2, and Cr_2CF_2 and $Cr_2C(OH)_2$ will translate into Cr_2CO_2 even if they were generated first during the etching reactions [31].

Ferro-magnetism is not always maintained in Cr_2C due to different surface terminations. For instance, Cr_2CF_2 is non-magnetic [9] while surface termination with O turns it into a ferromagnetic ground state [32]. Double-M (formulated as M′M″C, where M′(W) and M″(Cr) are two different early transition metals) 2D carbides (M′M″Xene) such as Mo_2VC_2, Mo_2NbC_2, Cr_2VC_2, Cr_2NbC_2 have been synthesized by Anasori *et al.*[33]. The layering due to different size of M atoms will be even more pronounced [33, 34] and it was found to be energetically more stable than their solid-solution counterparts for certain combinations of transition metals.

Most of MXenes are metallic, and they can be transformed into a semiconductor after surface passivation with fluoride and oxygen. The surface functionalization plays a key role in MXenes electronic snd magnetic prop-

erties. Oxygen passivated double-M 2D carbide $WCrCO_2$ shows tunable electronic properties by applying strain or electric field. Although 2DM hold significant potential for many applications, it will be necessary to tune their intrinsic properties. Several approaches have been considered to change the electronic structure of 2DM such as substitutional doping, defect engineering, application of an electric field or strain, surface functionalization by adatoms, or by altering the edge states [35–70].

Motivated by the reasons discussed above, we explore the structural and electronic properties of WCrC and $WCrCO_2$ monolayers. Using first-principle calculations, we investigate the effect of in-plane strain and electric field on the electronic properties of $WCrCO_2$ monolayer. In addition, the effect of out-of-plane strain on the $WCrCO_2$ bilayer is investigated. We found that 2D WCrC and $WCrCO_2$ MXenes are promising materials with semi-metallic character exhibiting an interesting narrow band gap.

II. METHOD

Our approach is based on Density functional theory (DFT) within the generalized gradient approximation for the exchange-correlation functional as proposed by Perdew-Burke-Ernzerhof (GGA-PBE) [71], along with norm-conserving pseudopotentials [72] as implemented in OpenMX package [73]. The eigenvalues and eigenfunctions of the Kohn-Sham equations are obtained self-consistently using norm-conserving pseudopotentials, and pseudoatomic orbitals (PAOs)[74, 75]. The energy cutoff was taken 400 Ry with a plane-wave basis set. The wave functions are expanded as a linear combination of multiple pseudoatomic orbitals (LCPAOs). The integration over the **k**-point mesh was performed using $23 \times 23 \times 1$ Monkhorst-Pack scheme for the primitive unit cell [76]. Double-M 2D carbides WCrC and $WCrCO_2$ monolayers are modelled as a periodic slab with a large vacuum layer (20 Å) between them in order to avoid interaction between adjacent layers. The ground state structure was obtained by using a quasi-Newton algorithm and it was relaxed until the residual forces on the atoms becomes smaller than 1 meV/Å. In order to accurately describe the van der Waals (vdW) interaction in $WCrCO_2$, we adopted the empirical correction method presented by Grimme (DFT-D2) [77] PHONOPY code[78] was used to obtain the vibrational properties which is based on the finite-displacement method. *Ab initio* molecular dynamics (AIMD) simulations were also carried out to examine the thermal stability of the double-M 2D carbides WCrC and $WCrCO_2$ monolayers by using $5\times5\times1$ super cell at room temperature (300 K) with total simulation time of 3 ps with 2 fs time steps.

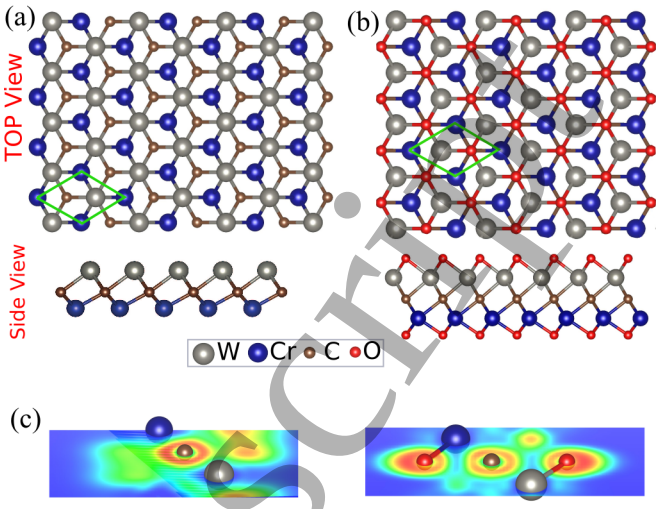

FIG. 1. Top and side view of the atomic structure of the double-M 2D carbides (a) WCrC and (b) $WCrCO_2$ monolayers, with its hexagonal primitive unit cell indicated by the green parallelogram. Gray, dark blue, brown and red balls represent W, Cr, C and O atoms. (c) Contour plot of the electron localization function (ELF) of the double-M 2D carbides WCrC (left) and $WCrCO_2$ (right). Red (blue) color indicate high (low) electron density.

III. PRISTINE WCRC AND $WCRCO_2$ MONOLAYERS

WCrC and $WCrCO_2$ monolayers crystallize in a hexagonal crystal structure and the unit cell contains two transition metal atoms (W and Cr) and one carbon (C) atom. After geometric optimization of WCrC, we used =O functionalization in order to realize $WCrCO_2$ in four different crystal structures [23]. In the present study we considered only the most favorable configuration which has the functional groups located on top of the hollow site of the carbon atom. Figs. 1(a) and (b) show top and side view of the optimized crystal structures of, respectively, pristine WCrC and $WCrCO_2$ monolayers with its hexagonal primitive unit cell, indicated by the green parallelogram. The lattice parameters of WCrC and $WCrCO_2$ are found to be 2.90 and 2.79 Å, respectively. Each C atom is covalently bonded with neighboring W and Cr atoms, and d_{M-C} is the bond length between W and Cr with C atom which is given in Table I. The distance between the uppermost and lowermost atomic layers along the c-axis is the thickness (d). The thickness of WCrC and $WCrCO_2$ monolayers are calculated to be 2.25 and 2.60 Å, respectively.

To investigate the charge transfer, we plot the electron localization function (ELF). The contours illustrate ELF of WCrC (left) and $WCrCO_2$ (right) in Fig. 1(c). We see that a high charge density is found around the C atom, which indicates a charge transfer from W and Cr atoms to C atom resulting in covalent bonding. The

Bader charge analysis technique [79] was employed to probe charge gain and loss. The difference charge density ($\Delta\rho$) is defined as

$$\Delta\rho = \rho_{WCrC} - \rho_W - \rho_{Cr} - \rho_C \quad (1)$$

where ρ_{WCrC}, ρ_W, ρ_{Cr} and ρ_C represents the charge densities of the WCrC monolayer and isolated atoms, respectively. Based on Bader charge analysis, each C atom gains about 1.41 e from the adjacent W and Cr atoms, while W and Cr atoms loses 0.66 and 0.76 e, respectively in WCrC. While in $WCrCO_2$, each O and C atom gain about 0.9 e and 1.23 e from the adjacent W and Cr atoms, respectively, while W and Cr atoms loses 1.56 and 1.35 electron. The charge redistribution in WCrC and $WCrCO_2$ is due to the different electro-negativities of 2.36 (W), 1.66 (Cr), 2.55 (C) and 3.44 (O). Cohesive energy, which is defined as the energy required to separate the condensed material into isolated free atoms, is one of the most important physical parameters in quantifying the stability of materials. The cohesive energy per atom was calculated using the following equation:

$$E_{coh} = (E_W + E_{Cr} + E_C + 2E_O) - E_{MXenes})/n_{tot} \quad (2)$$

where E_W, E_{Cr}, E_C and E_O represent the energies of isolated single W, Cr, C and O atoms; E_{MXenes} represents the total energy of the MXene, and total number of atoms (n_{top}=3,5 for pristine and =O functionalization), respectively. The cohesive energy of WCrC and $WCrCO_2$ monolayers are found to be 3.58 and 3.33 eV/atom, respectively, which indicates that $WCrCO_2$ is more favorable than pristine WCrC.

From the vibrational properties we obtain the dynamical stability of the new predicted structures. The phonon dispersion along the high symmetry points (Γ, M, K) for WCrC and $WCrCO_2$ is shown in Figs. 2(a) and (b), respectively. There are one tungsten, one chromium, and one carbon atoms, in the primitive unit cell and therefore, the WCrC phonon spectrum consists of 9 phonon branches: 3 acoustic and 6 optical. Based on the basal plane symmetry of 2DM the 6 optical phonon branches consist of two singly degenerate (237.9 and 670.9 cm^{-1}) and two doubly degenerate (187.5 and 699.6 cm^{-1}) branches, the acoustic phonon branches consist of doubly degenerate in-plane transverse (TA) and longitudinal (LA) phonon branches at the Γ point. $WCrCO_2$ has five atoms in the primitive unit cell and therefore the phonon spectrum includes 15 phonon branches: 3 acoustic and 12 optical. Optical phonons include four singly degenerate (239.5, 629.9, 692.3, 754.7 cm^{-1}) and four doubly degenerate (131.5, 426.5, 474.8, 587.4 cm^{-1}). Notice that all phonon modes have real eigenfrequencies indicating that pristine WCrC and =O functionalization $WCrCO_2$ are dynamically stable Thus it is expected that synthesis of the double-M MXene WCrC and $WCrCO_2$ are possible as a freestanding monolayers. Additionally,

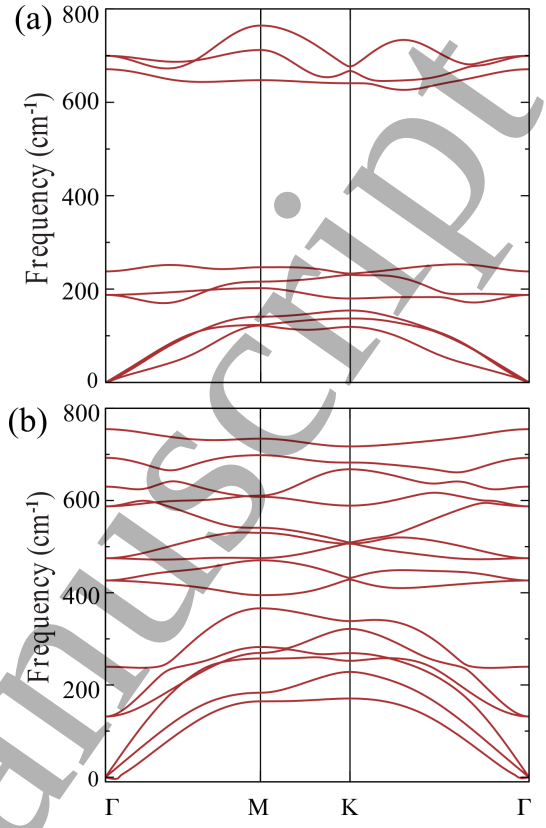

FIG. 2. The phonon band structure of (a) WCrC and (b) $WCrCO_2$ monolayers.

TABLE I. The calculated lattice constant (a), bonding distance between W/Cr and C ($d_{W/Cr-C}$), bonding distance between W/Cr and O ($d_{W/Cr-O}$), thickness (d), and cohesive energy per atom (E_{coh}) for the ground state configuration of the WCrC and $WCrCO_2$ monolayers.

	a (Å)	d_{W-C} (Å)	d_{Cr-C} (Å)	d_{W-O} (Å)	d_{Cr-O} (Å)	d (Å)	E_{coh} (eV)
WCrC	2.90	2.11	1.93	-	-	2.25	6.94
$WCrCO_2$	2.79	2.12	2.11	2.07	1.91	2.60	5.81

thermal stability of WCrC and $WCrCO_2$ monolayers are further examined by *Ab initio* molecular dynamics simulations (AIMD) using a 5 × 5 × 1 supercell at 300 K. AIMD simulation for both monolayers at 300 K is shown in Fig. S1 of the supplementary information (SI), where the optimized structures are indicated in the inset. The thermal dynamic investigations are started with the optimized structures at 0 K. The temperature was increased to 300 K (room temperature) within 2 ps. As can be noticed from the snapshots, apart from minor distortions, the crystal structures of both WCrC and$WCrCO_2$ monolayers are preserved, further confirming the stability even at least up to 300 K.

Next we investigated the electronic band dispersion of WCrC and $WCrCO_2$ monolayers. Due to valence d-

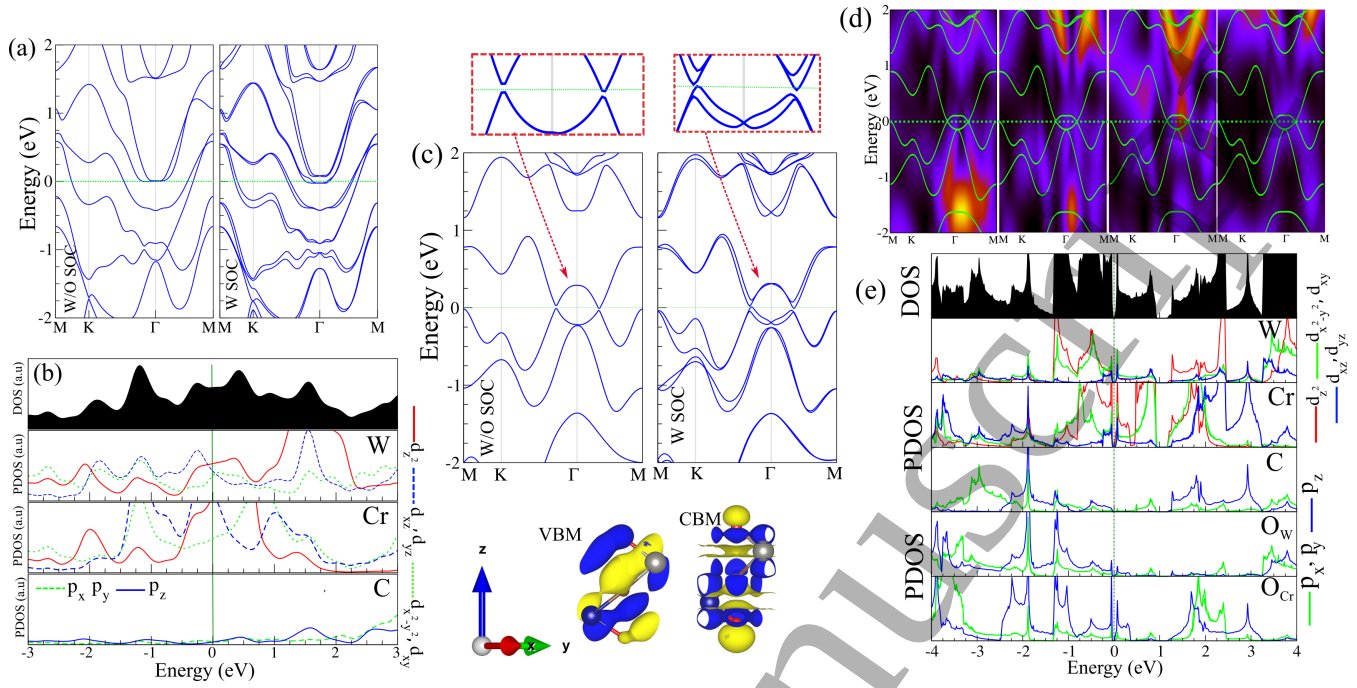

FIG. 3. (a) Electronic band structure without and with spin-orbital coupling (SOC) and (b) DOS and PDOS of WCrC monolayer. (c) Electronic band structure without and with SOC of $WCrCO_2$ monolayer. Zoom of the band structure indicated in the top panel. Charge densities of the valance band maximum (VBM) and conduction band minimum (CBM) orbitals are shown in the bottom panel. The blue and yellow regions represent charge accumulation and depletion, respectively. (d) Intensity map of electronic band structure and (e) DOS and PDOS of $WCrCO_2$ monolayer. The oxygen atom which is bonded to W and Cr atoms, are labeled as O_W and O_Cr respectively. Zero of energy is set at the Fermi-level.

electrons of W and Cr atoms, spin-orbit coupling (SOC) effects are expected to be significant which is included within PBE+SOC. As shown in Fig. 3(a), WCrC is metallic based on PBE, when we consider PBE+SOC the metallic character is preserved but the energy bands around the Fermi-level split with energy splitting of 30 meV. In order to explain the origin of the electronic states of WCrC, we have calculated the density of states (DOS) and projected PDOS, as shown in Fig. 3 (b). From the PDOS of WCrC, we see that the metallic state near the Fermi-level originates from W-(d_{z^2}, $d_{x^2-y^2}$,d_{z^2}) and Cr-(d_{xz}, d_{yz},d_{z^2}) orbitals, while the C atom orbitals do not contribute. The electronic band structure of $WCrCO_2$ with and without considering the SOC is shown in Fig. 3(c) and a zoom of the band structure around the Fermi-level is shown in the top panel. Notice that, after chemical modification with O atoms, the metallic character disappears and exhibit a semi-metal without SOC. In addition, a dual band gap opened with narrow values of 45 and 40 meV at the left and right of the Γ point, respectively. While the valence band maximum (VBM) and conduction band minimum (CBM) are located around the Γ point. The charge densities of the VBM and CBM orbitals are shown in the bottom panel of Fig. 3(c), where the blue and yellow regions represent the charge accumulation and depletion, respectively. When including the SOC effect, the electronic bands split and the dual band gaps are changed to 30 and 45 meV at left and right of the Γ point, respectively. We see that there is only a small SOC effect on the electronic structure of WCrC and $WCrCO_2$ monolayers. Furthermore, from DOS and PDOS of $WCrCO_2$ in Fig. 3(e), we notice that the VBM and CBM originates from Cr-(d_{z^2}) and O-(p_z) orbital states. Notice that the W-(d_{z^2} and $d_{x^2-y^2}$) orbitals have a small contribution in VBM and CBM, while the p orbital of C atom does not contribute at all. The intensity map of the electronic band structure is show, in Fig. 3(d). Energy bands around the Fermi-level mainly originates from Cr and O_{Cr} atoms (O bonded to Cr) and slightly W atom. We have additionally computed electronic properties of $WCrCO_2$ monolayer using the HSE06 functional. As shown in Fig. S2, semi-metallic properties of the $WCrCO_2$ was preserved.

Spin-polarized density functional calculations indicate that the ground states of the majority of the pristine and functionalized WCrC monolayer are nonmagnetic because of the strong covalent bonding between the transition metal and the O element as well as the attached chemical groups. In here we investigate the crystal symmetry of the d orbital states in $WCrCO_2$ monolayer. In functionalized $WCrCO_2$, each transition metal is surrounded by C atoms and the terminating chemical

groups, which form a distorted octahedral crystal field around the transition metal (W and Cr). The schematic energy levels for d orbitals of a transition metal under octahedral coordination environment, which are found in $WCrCO_2$ structure is shown in Fig. S3(a). The schematic of crystal field is shown in the inset. The DOS and PDOS of $WCrCO_2$ monolayer is shown in Fig. S3(b). The resulting nearly octahedral crystal field splits the d orbital of the transition metal into three t_2g (d_{xy}, d_{yz}, and d_{xz}) and two e_g ($d_{z^2}, d_{x^2-y^2}$ and d_{z^2}) orbital sub-states in a perfect octahedral crystal field. Because of the orbital shapes, the e_g-orbital manifold is energetically higher than the t_2g-orbital manifold. Therefore, electrons occupy first the t_2g orbitals before entering the e_g-orbitals. In addition, we investigate effects of correlation by varying the value of the Hubbard U, since the exact value of U for $WCrCO_2$ is not known. Electronic band structure of $WCrCO_2$ monolayer with respect to Hubbard parameter U without considering SOC and with considering SOC are shown in Figs. S4(a) and (b), respectively. The left and right panels are with respect to U=2 eV and U=3 eV, respectively. The correlation effects on the electronic properties of $WCrCO_2$ are insignificant and we can see that the $WCrCO_2$ still maintains the semi-metallic character with dual narrow band gaps about 30 meV (without considering SOC) and 45 meV (with considering SOC) feature even when considering the effect of Hubbard U.

IV. ELECTRIC FIELD TUNING OF $WCrCO_2$ MONOLAYER

From the perspective of potential device applications, the ability to tune the electronic properties by e.g. controlling the Fermi-level via electric field is highly desirable. The presence of buckling in $WCrCO_2$, leads to a potential difference between the two atomic sublayers, which is useful in tuning the electronic properties. The electronic band structure of $WCrCO_2$ monolayer as function of electric field parallel and anti-parallel to the z-axis are shown in Figs. 4(a,b) when including SOC.

With increasing electric field from 0.2 to 1.0 V/Å, the two VBM around the Γ-point shift towards the Γ point and the spectrum bands become more tilted, while the CBM decreases in energy (see Fig 4.(a)). The effect of the electric field for the band structure around the Γ-point is to tilt the spectrum and the tilt is opposite for parallel and anti-parallel electric field. For parallel field the Fermi energy moves inside the CB resulting in field induced electron doping. The small splitting is only slightly influenced. For anti-parallel electric field the VB moves above the Fermi energy and we see a small hole doping. The VBM around the Γ-point moves up (down) for (anti-) parallel field. Thus electric gating allows us to electrically dope the system and transforms it from a bad conductor (i.e. Fermi energy inside the small band gap) to a conductor.

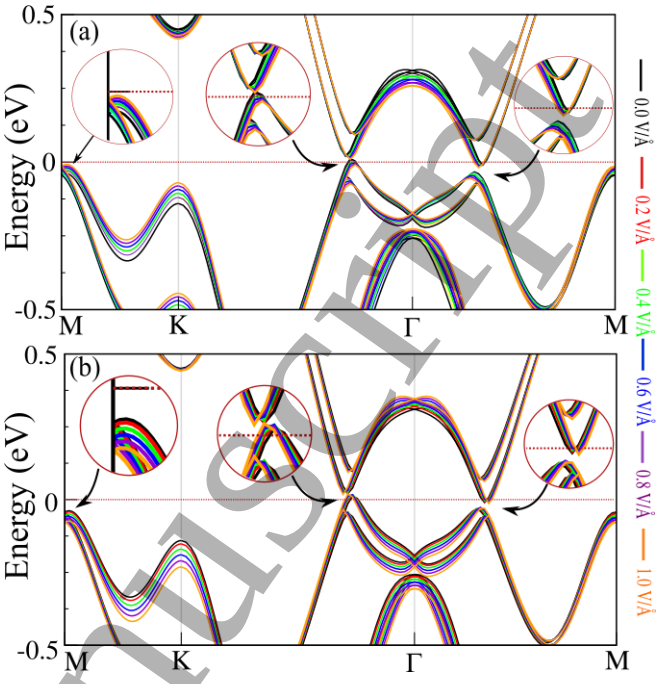

FIG. 4. Electronic band structure of $WCrCO_2$ monolayer as function of (a) parallel and (b) anti-parallel electric field to the z-axis with SOC. Zero of energy is set to the Fermi level.

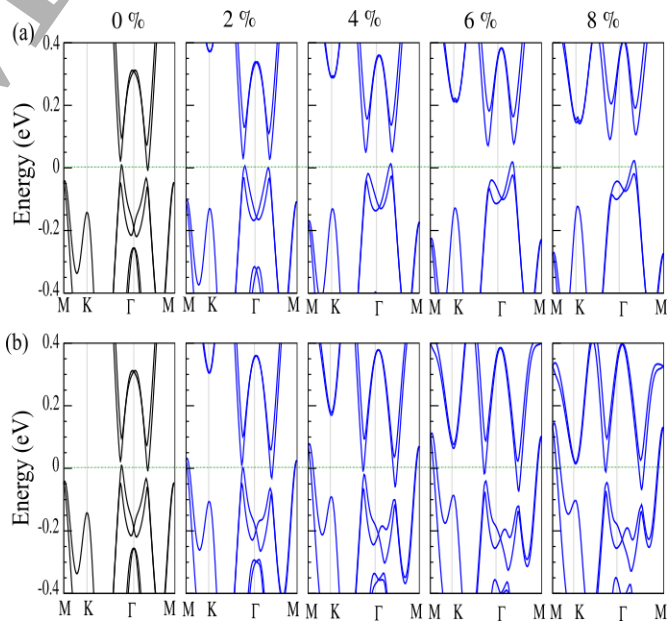

FIG. 5. Electronic band structure of $WCrCO_2$ monolayer as a function of (a) uniaxial and (b) biaxial strain when including SOC. Zero of energy is set to the Fermi level.

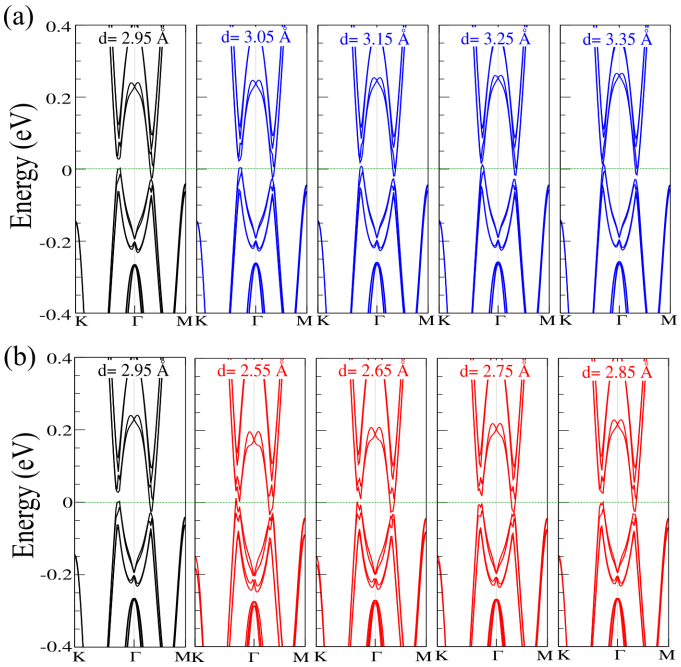

FIG. 6. Electronic band structure of $WCrCO_2$ bilayer as a function of interlayer distance. Zero of energy is set to the Fermi level.

V. STRAINING $WCRCO_2$

Strain engineering is a robust method to tune the electronic properties and its topological nature. Here, we investigate the effect of in-plane strain on the electronic properties of $WCrCO_2$ monolayer. The strain is defined as $\varepsilon = (a - a_0)/a_0 \times 100$, where a (a_0) is strained (non-strained) lattice constant. The uniaxial strain is applied along the zigzag direction, while biaxial strain is applied along the a-b axis. The electronic band structure of $WCrCO_2$ monolayer as function of uniaxial and biaxial strain with SOC is shown in Fig. 5(a). Under uniaxial strain, the band gap changes from 30 and 45 meV (at 0%) to 30 and 30 meV (at +2%) on, respectively, the left and right of Γ-point. Notice that the VBM continuously shifts towards the Fermi-level resulting in hole doping, while the CBM increases in energy, leading to an increase of the band gap. The band gap on the left (right) of Γ-point increases to 70 (65), 110 (95) and 135 (130) meV, for strain of +4, +6 and +8%, respectively. While, under biaxial strain,the VBM at M-point, continuously shift upwards resulting in the hole doping while CB around the Γ-point moves below E_F. This leads to a semi-metallic character.

Out-of plane strain, i. e. pressure, can change the interlayer distance and thus the vdW interaction, which may induce electronic state transitions. We determine the lowest energy stacking configuration of $WCrCO_2$ bilayer, including structural optimization. The different stacking patterns including $AA1$, $AA1$, $AB1$ and $AB2$ of $WCrCO_2$ bilayer that we considered are shown in Fig. S5. The relative total energy of four stacking patterns for the $WCrCO_2$ bilayer is shown in Fig. S5. Side views of the stacking structures are shown in the inset. Our results show that the $AA1$ stacking is most stable. The electronic band structure with SOC of $WCrCO_2$ bilayer as a function of interlayer distance are shown in Figs. 6(a,b). For $WCrCO_2$ bilayer, the equilibrium interlayer distance is 2.95 Å. Comparing with $WCrCO_2$ monolayer, we see that the dual band gaps decreases to 30 and 5 meV at left and right of Γ-point, respectively. Notice that with increasing strain the interlayer distance of the two layers of $WCrCO_2$ changes from 3.05 to 3.35 Å(see in Fig. 6(a)). Our result show that the band gap decrease to 25 meV (at 3.05 Å) and reaches zero (at 3.35 Å) at the left of the Γ-point. While, at the right of the Γ-point, the situation differs and band gap increases from 45 (at 3.05 Å) to 50 meV (at 3.35 Å). The reason is that the increased interlayer distance weakens the interlayer coupling, resulting in $WCrCO_2$ bilayer to keep their individual electronic properties. Conversely, one can see that the band gap is approximately constant when the interlayer distance increases. While, with decreasing interlayer distance, the band gaps are in the range of 20-30 meV and 5-10 meV in the left and right of the Γ-point, respectively. Our results show that the electronic structure of $WCrCO_2$ bilayer under increasing and decreasing of interlayer distance preserved its metal character.

VI. CONCLUSION

In conclusion, we investigated the structural, electronic and dynamical properties of WCrC and $WCrCO_2$ monolayers as well as the effects of in- and out-of-plane strain and electric field using first-principle calculations. Firstly, the optimized WCrC and $WCrCO_2$ crystal structures are found to be thermodynamically and dynamically stable. The electronic structure of WCrC indicates that it is a metal which is fundamentally modified with -O termination and a band gap is opened. Additionally, electronic properties of $WCrCO_2$ monolayer under a positive electric field and applying in-plane strain are also studied. The obtained electronic properties show that the dual band gap is preserved under an parallel and anti parallel electric field. The band gap of $WCrCO_2$ monolayer increases under uniaxial strain while it becomes metallic under tensile strain. The out-of-plane strain effect on $WCrCO_2$ bilayer also investigate in this study. Increasing/decreasing the inter-layer distances of $WCrCO_2$ bilayer effects the band gap value, but the semi-metal character retains. We expect that our theoretical study will stimulate further experimental research on this material in the future. The present findings is expected to promote more interest in developing MXenes. Moreover, with the existence of a tunable band gap by electric field,

charging and strain $WCrCO_2$ is highly desirable for its use in nanoscale device applications.

VII. ACKNOWLEDGMENTS

This work was supported by the National Research Foundation of Korea(NRF) grant funded by the Korea government(MSIT)(NRF-2017R1A2B2011989). In addition, this work was supported by the Flemish Science Foundation (FW0-Vl).

* Bafekry.asad@gmail.com

[1] M. Naguib, M. Kurtoglu, V. Presser, J. Lu, J. Niu, M. Heon, L. Hultman, Y. Gogotsi, and M. W. Barsoum, Advanced Materials **23**, 4248 (2011).
[2] M. Naguib, V. N. Mochalin, M. W. Barsoum, and Y. Gogotsi, Advanced Materials **26**, 992 (2014).
[3] K. Hantanasirisakul and Y. Gogotsi, Advanced Materials **30**, 1804779 (2018).
[4] B. Anasori, M. R. Lukatskaya, and Y. Gogotsi, Nature Reviews Materials **2**, 16098 (2017).
[5] Y. Gogotsi and B. Anasori, ACS Nano **13**, 8491 (2019).
[6] B. Anasori and Y. Gogotsi, in *2D Metal Carbides and Nitrides (MXenes)* (Springer, 2019) pp. 3–12.
[7] N. C. Frey, J. Wang, G. I. Vega Bellido, B. Anasori, Y. Gogotsi, and V. B. Shenoy, ACS Nano **13**, 3031 (2019).
[8] Y. Liang, M. Khazaei, A. Ranjbar, M. Arai, S. Yunoki, Y. Kawazoe, H. Weng, and Z. Fang, Physical Review B **96**, 195414 (2017).
[9] M. Khazaei, A. Ranjbar, M. Arai, T. Sasaki, and S. Yunoki, Journal of Materials Chemistry C **5**, 2488 (2017).
[10] A. D. Dillon, M. J. Ghidiu, A. L. Krick, J. Griggs, S. J. May, Y. Gogotsi, M. W. Barsoum, and A. T. Fafarman, Advanced Functional Materials **26**, 4162 (2016).
[11] F. Shahzad, M. Alhabeb, C. B. Hatter, B. Anasori, S. M. Hong, C. M. Koo, and Y. Gogotsi, Science **353**, 1137 (2016).
[12] J. Liu, H.-B. Zhang, R. Sun, Y. Liu, Z. Liu, A. Zhou, and Z.-Z. Yu, Advanced Materials **29**, 1702367 (2017).
[13] C. Zhang, B. Anasori, A. Seral-Ascaso, S.-H. Park, N. McEvoy, A. Shmeliov, G. S. Duesberg, J. N. Coleman, Y. Gogotsi, and V. Nicolosi, Advanced Materials **29**, 1702678 (2017).
[14] G. Ying, A. D. Dillon, A. T. Fafarman, and M. W. Barsoum, Materials Research Letters **5**, 391 (2017).
[15] C. J. Zhang, S. Pinilla, N. McEvoy, C. P. Cullen, B. Anasori, E. Long, S.-H. Park, A. Seral-Ascaso, A. Shmeliov, and D. Krishnan, Chemistry of Materials **29**, 4848 (2017).
[16] C. Si, J. Zhou, and Z. Sun, ACS Applied Materials & Interfaces **7**, 17510 (2015).
[17] H. Kumar, N. C. Frey, L. Dong, B. Anasori, Y. Gogotsi, and V. B. Shenoy, ACS Nano **11**, 7648 (2017).
[18] Y. Zhang and F. Li, Journal of Magnetism and Magnetic Materials **433**, 222 (2017).
[19] K. Zhang, M. Di, L. Fu, Y. Deng, Y. Du, and N. Tang, Carbon **157**, 90 (2020).
[20] S. Zhao, W. Kang, and J. Xue, Applied Physics Letters **104**, 133106 (2014).
[21] D. Magne, V. Mauchamp, S. Célérier, P. Chartier, and T. Cabiocéh, Physical Chemistry Chemical Physics **18**, 30946 (2016).
[22] J. Yang, X. Zhou, X. Luo, S. Zhang, and L. Chen, Applied Physics Letters **109**, 203109 (2016).
[23] B. Akgenc, Computational Materials Science **171**, 109231 (2020).
[24] K. D. Pham, N. V. Hieu, L. M. Bui, I. V. Ershov, N. N. Hieu, H. V. Phuc, B. D. Hoi, L. T. Phuong, L. M. Duc, and M. Idrees, Materials Research Express **6**, 065910 (2019).
[25] N. C. Frey, A. Bandyopadhyay, H. Kumar, B. Anasori, Y. Gogotsi, and V. B. Shenoy, ACS Nano **13**, 2831 (2019).
[26] Y. Lee, Y. Hwang, S. B. Cho, and Y.-C. Chung, Physical Chemistry Chemical Physics **16**, 26273 (2014).
[27] C. Xu, L. Wang, Z. Liu, L. Chen, J. Guo, N. Kang, X.-L. Ma, H.-M. Cheng, and W. Ren, Nature Materials **14**, 1135 (2015).
[28] J. Halim, S. Kota, M. R. Lukatskaya, M. Naguib, M.-Q. Zhao, E. J. Moon, J. Pitock, J. Nanda, S. J. May, and Y. Gogotsi, Advanced Functional Materials **26**, 3118 (2016).
[29] D. Wu, S. Wang, S. Zhang, J. Yuan, B. Yang, and H. Chen, Physical Chemistry Chemical Physics **20**, 18924 (2018).
[30] R. Peng, Y. Ma, Q. Wu, B. Huang, and Y. Dai, Nanoscale **11**, 11413 (2019).
[31] Y. Cheng, L. Wang, Y. Li, Y. Song, and Y. Zhang, The Journal of Physical Chemistry C **123**, 15629 (2019).
[32] J.-T. Ye, L. Wang, H.-Q. Wang, X.-M. Pan, H.-M. Xie, and Y.-Q. Qiu, The Journal of Physical Chemistry C **122**, 18850 (2018).
[33] B. Anasori, Y. Xie, M. Beidaghi, J. Lu, B. C. Hosler, L. Hultman, P. R. Kent, Y. Gogotsi, and M. W. Barsoum, ACS Nano **9**, 9507 (2015).
[34] L. Wang, P. Hu, Y. Long, Z. Liu, and X. He, Journal of Materials Chemistry A **5**, 22855 (2017).
[35] A. Bafekry and M. Neek-Amal, Phys. Rev. B **101**, 085417 (2020).
[36] M. M. Obeid, H. R. Jappor, K. Al-Marzoki, D. Hoat, T. V. Vu, S. J. Edrees, Z. M. Yaseen, and M. M. Shukur, Computational Materials Science **170**, 109201 (2019).
[37] A. Bafekry, C. Stampfl, M. Ghergherehchi, and S. F. Shayesteh, Carbon **157**, 371 (2020).
[38] T. V. Vu, N. V. Hieu, H. V. Phuc, N. N. Hieu, H. Bui, M. Idrees, B. Amin, and C. V. Nguyen, Applied Surface Science **507**, 145036 (2020).
[39] A. Bafekry, M. Ghergherehchi, and S. Farjami Shayesteh, Phys. Chem. Chem. Phys. **21**, 10552 (2019).
[40] D. D. Vo, T. V. Vu, N. V. Hieu, N. N. Hieu, H. V. Phuc, N. T. T. Binh, L. T. T. Phuong, M. Idrees, B. Amin, and C. V. Nguyen, Phys. Chem. Chem. Phys. **21**, 25849 (2019).
[41] M. Yagmurcukardes, C. Sevik, and F. M. Peeters, Phys. Rev. B **100**, 045415 (2019).
[42] A. Bafekry, C. Stampfl, S. F. Shayesteh, and F. M. Peeters, Advanced Electronic Materials **5**, 1900459 (2019).

[43] H. U. Din, M. Idrees, A. Albar, M. Shafiq, I. Ahmad, C. V. Nguyen, and B. Amin, Phys. Rev. B **100**, 165425 (2019).
[44] D. Kiymaz, M. Yagmurcukardes, A. Tomak, H. Sahin, R. T. Senger, F. M. Peeters, H. M. Zareie, and C. Zafer, Nanotechnology **27**, 455604 (2016).
[45] A. Bafekry, S. Farjami Shayesteh, and F. M. Peeters, Phys. Chem. Chem. Phys. **21**, 21070 (2019).
[46] M. M. Obeid, H. R. Jappor, K. Al-Marzoki, I. A. Al-Hydary, S. J. Edrees, and M. M. Shukur, RSC Advances **9**, 33207 (2019).
[47] A. Bafekry, S. Farjami Shayesteh, M. Ghergherehchi, and F. M. Peeters, Journal of Applied Physics **126**, 144304 (2019).
[48] M. Shahrokhi and C. Leonard, Journal of Alloys and Compounds **693**, 1185 (2017).
[49] A. Bafekry, C. Stampfl, and F. M. Peeters, Sci. Rep. **10**, 1 (2020).
[50] M. M. Obeid, Applied Surface Science **508**, 144824 (2020).
[51] A. Bafekry, Physica E: Low-dimensional Systems and Nanostructures **118**, 113850 (2020).
[52] K. D. Pham, N. N. Hieu, H. V. Phuc, I. A. Fedorov, C. A. Duque, B. Amin, and C. V. Nguyen, Applied Physics Letters **113**, 171605 (2018).
[53] A. Bafekry, C. Stampfl, B. Akgenc, B. Mortazavi, M. Ghergherehchi, and C. V. Nguyen, Phys. Chem. Chem. Phys. **22**, 6418 (2020).
[54] P. T. T. Le, N. N. Hieu, L. M. Bui, H. V. Phuc, B. D. Hoi, B. Amin, and C. V. Nguyen, Phys. Chem. Chem. Phys. **20**, 27856 (2018).
[55] A. Bafekry, C. Stampfl, B. Akgenc, and M. Ghergherehchi, Phys. Chem. Chem. Phys. **22**, 2249 (2020).
[56] F. Iyikanat, M. Yagmurcukardes, R. T. Senger, and H. Sahin, J. Mater. Chem. C **6**, 2019 (2018).
[57] M. Yagmurcukardes, Phys. Rev. B **100**, 024108 (2019).
[58] A. Bafekry, B. Akgenc, S. F. Shayesteh, and B. Mortazavi, Applied Surface Science **505**, 144450 (2020).
[59] M. Yagmurcukardes, S. Ozen, F. Iyikanat, F. M. Peeters, and H. Sahin, Phys. Rev. B **99**, 205405 (2019).
[60] M. Shahrokhi, Applied Surface Science **390**, 377 (2016).
[61] A. Bafekry, C. Stampfl, and S. Farjami Shayesteh, ChemPhysChem **21**, 164 (2020).
[62] M. Shahrokhi and C. Leonard, Journal of Alloys and Compounds **682**, 254 (2016).
[63] A. Bafekry, S. F. Shayesteh, and F. M. Peeters, Journal of Applied Physics **126**, 215104 (2019).
[64] J. Zhou, M. Khazaei, A. Ranjbar, V. Wang, T. D. Khne, K. Ohno, Y. Kawazoe, and Y. Liang, J. Mater. Chem. C , (2020).
[65] A. Bafekry, B. Mortazavi, and S. F. Shayesteh, Journal of Magnetism and Magnetic Materials **491**, 165565 (2019).
[66] M. Khazaei, J. Wang, M. Estili, A. Ranjbar, S. Suehara, M. Arai, K. Esfarjani, and S. Yunoki, Nanoscale **11**, 11305 (2019).
[67] N.-A. M. Bafekry, A. and F. M. Peeters, Phys. Rev. B **101**, 085417 (2020).
[68] J. Yu, M. Khazaei, N. Umezawa, and J. Wang, J. Mater. Chem. C **6**, 5803 (2018).
[69] M. Khazaei, M. Arai, T. Sasaki, M. Estili, and Y. Sakka, Science and Technology of Advanced Materials **15**, 014208 (2014).
[70] a. M. G. A. Bafekry, C. Stampfl, Nanotechnology **101**, 085417 (2020).
[71] J. P. Perdew, K. Burke, and M. Ernzerhof, Physical Review Letters **77**, 3865 (1996).
[72] N. Troullier and J. L. Martins, Physical Review B **43**, 1993 (1991).
[73] T. Ozaki, K. Nishio, and H. Kino, Phys. Rev. B **81**, 035116 (2010).
[74] T. Ozaki, Physical Review B **67**, 155108 (2003).
[75] T. Ozaki and H. Kino, Physical Review B **69**, 195113 (2004).
[76] H. J. Monkhorst and J. D. Pack, Physical Review B **13**, 5188 (1976).
[77] S. Grimme, Journal of Computational Chemistry **27**, 1787 (2006).
[78] D. Alfè, Computer Physics Communications **180**, 2622 (2009).
[79] G. Henkelman, A. Arnaldsson, and H. Jónsson, Computational Materials Science **36**, 354 (2006).